



Hydrogen spillover effect tuning the rate-determining step of hydrogen evolution over Pd/Ir hetero-metallene for industry-level current density

Kai Deng, Zilong Lian, Wenxin Wang, Jiabao Yu, Qiqi Mao, Hongjie Yu, Ziqiang Wang, Liang Wang, Hongjing Wang*

State Key Laboratory Breeding Base of Green-Chemical Synthesis Technology, College of Chemical Engineering, Zhejiang University of Technology, Hangzhou 310014, PR China

ARTICLE INFO

Keywords:

Metallene, Pt-group metals
Hydrogen evolution reaction
Hydrogen spillover
Industry-level current density

ABSTRACT

Despite the fruitful achievements in the development of high-performance catalysts, most of materials still suffer limited HER kinetics and poor durability in harsh acidic media, especially at high current densities. In this work, a Pd nanoparticles/Ir metallene heterojunction structure (Pd/Ir hetero-metallene) were successfully prepared by a facile co-reduction method. The hydrogen spillover bridging H^+ adsorption/ H_2 desorption process occurring at the Pd/Ir interface results in the rate-determining step change to a Tafel step, which accelerates the HER kinetics. The Pd/Ir hetero-metallene has a relatively low $\Delta G_{H_{ads}}$ (-0.19 eV), which allows for rapid adsorption of H^+ and release of H_2 , thus greatly improving the performance of HER. As a result, the Pd/Ir hetero-metallene exhibits remarkable HER performance with ultra-low overpotentials of only 69 and 133 mV to reach 500 and 1000 $mA\ cm^{-2}$, a small Tafel slope of 21 $mV\ dec^{-1}$, and superb stability.

1. Introduction

H_2 , with its high energy density and zero-emission characteristics, has become an ideal energy carrier to replace traditional fossil fuels and move towards a carbon neutrality society in the future [1–4]. Electrochemical water splitting is an attractive method for producing high purity H_2 compared to conventional processing techniques [4–7]. To date, Pt has been considered the most advanced electrocatalyst for the hydrogen evolution reaction (HER) [8–11]. However, Pt still suffers from susceptibility to deactivation and poor durability, especially in harsh acidic media, which limits its large-scale commercialization [12, 13]. The efficiency of HER is also affected by the slow kinetics including the initial electrochemical hydrogen adsorption process (Volmer step, $H_3O^+ + M + e^- \rightleftharpoons M-H_{ads} + H_2O$) and the subsequent desorption process (Heyrovsky step, $H^+ + e^- + M-H_{ads} \rightleftharpoons M + H_2$ or Tafel step, $2 M-H_{ads} \rightleftharpoons 2 M + H_2$) [14,15]. Therefore, it is highly desirable to further develop efficient and robust HER electrocatalysts to meet the demands of industrial production.

From Sabatier's principle, the ideal HER catalyst should have a moderate interaction with hydrogen intermediate, i.e., the Gibbs free energy of adsorbed H ($\Delta G_{H_{ads}} \approx 0$) is neither too strong nor too weak [16–19]. Recently, hydrogen spillover effect in metal-supported

catalysis has been creatively proposed to improve the performance of HER [20,21]. It involves three steps: I) strong H_{ads} adsorption on metals ($\Delta G_{H-metal} < 0$), II) metal→support hydrogen spillover, and III) easy hydrogen desorption on supports ($\Delta G_{H-support} > 0$) [22,23]. Nevertheless, the large difference of the Fermi levels (E_f) between metal and support induces charge accumulation at the interface, which results in Schottky barrier and strong proton adsorption [24–26]. In this case, the hydrogen spillover process will overcome the high energy barrier as H_{ads} diffuses from the metal to support, which limited HER activity [27]. Ma et al. point out that the similar E_f between the metal and the support favors the electronic configuration, so the energy barrier for hydrogen spillover is expected to be significantly reduced, thus promoting HER kinetics [28]. Based on the above concepts, the metal and carrier are preferably chosen on either side of a typical "volcano diagram" and the $\Delta G_{H_{ads}}$ value is preferably close-to-zero. Pd and Ir, as Pt-based materials, are considered to be the best candidates according to the classic volcano curves [29–31]. They also present excellent intrinsic stability in harsh acidic catalytic environments [32,33]. To further improve the catalytic activity of Pd and Ir, the formation of low-dimensional nanostructures (e.g., two-dimensional (2D) nanosheets (NSs)) with a larger surface area is an effective approach [34–36]. As an emerging class of 2D NSs electrocatalysts, metallene with ultrathin lamellar structures have received

* Corresponding author.

E-mail address: hjw@zjut.edu.cn (H. Wang).

<https://doi.org/10.1016/j.apcatb.2024.124047>

Received 22 February 2024; Received in revised form 28 March 2024; Accepted 6 April 2024

Available online 7 April 2024

0926-3373/© 2024 Elsevier B.V. All rights reserved.

increasing attention [37–41]. In addition, compared to conventional metal nanoparticles (NPs), metallene offer improved electron transfer due to their high connectivity, which is advantageous for H_{ads} desorption on supports, thus improve the hydrogen spillover kinetics [42,43].

In this work, we designed a Pd NPs/Ir metallene heterojunction structure (Pd/Ir hetero-metallene), in which Pd NPs are uniformly distributed on an ultrathin 2D Ir metallene. The tiny difference in the E_f between Pd and Ir favors electron dilution and proton migration at the Pd/Ir interface, which improves hydrogen spillover kinetics. With the contribution of hydrogen spillover effect and unique metallene structure, the Pd/Ir hetero-metallene exhibits remarkable HER performance with only 133 mV overpotential required at 1000 mA cm^{-2} , a small Tafel slope of 21 mV dec^{-1} , and superb stability.

2. Experimental section

2.1. Chemicals and materials

Sodium tetrachloropalladate(II) (Na_2PdCl_4 , 99%) was obtained from Sigma-Aldrich. Iridium trichloride (IrCl_3 , 99%), 1-methyl-2-pyrrolidinone (NMP), WO_3 , formic acid (HCOOH , 88%), ethanol ($\text{C}_2\text{H}_5\text{OH}$), acetone ($\text{C}_3\text{H}_6\text{O}$), sulfuric acid (H_2SO_4) and nafion (5 wt%) were purchased from Aladdin. Commercial Pt/C (20 wt%) and RuO_2 were acquired from Alfa Aesar. All the chemicals were used without further purification.

2.2. Synthesis of Pd/Ir hetero-metallene

In a typical synthesis, a mixture of 0.75 mL of $\text{IrCl}_3 \cdot x\text{H}_2\text{O}$ (40 mM), 0.25 mL of Na_2PdCl_4 (40 mM), and 5 mL NMP was injected into a 30 mL glass vial and sonicated for 10 min. Subsequently, 1 mL of HCOOH is added to the above mixture, which is then heated in an oil bath at 95°C for 4 h. After cooling to room temperature, the black product was collected by centrifugation and washed four times with ethanol and acetone. The Ir metallene and Pd NPs were prepared by the same procedure described above with the addition of only $\text{IrCl}_3 \cdot x\text{H}_2\text{O}$ and Na_2PdCl_4 , respectively.

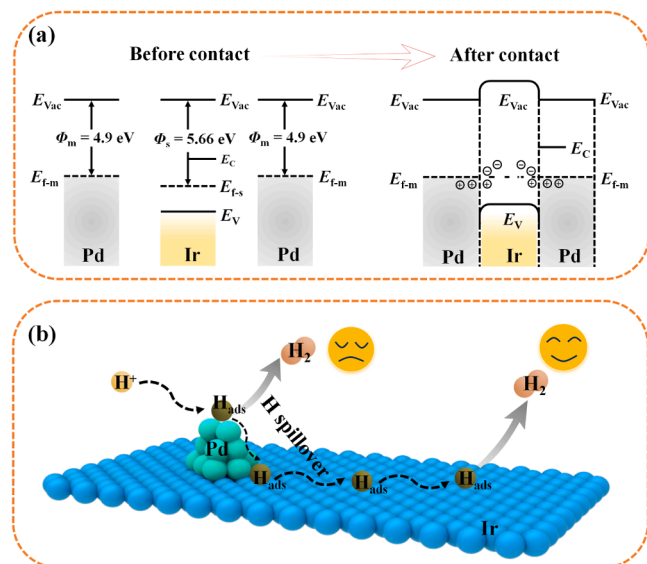


Fig. 1. (a) Schematic diagram of interfacial electron configuration in Pd/Ir hetero-metallene. (b) Illustration of hydrogen spillover phenomenon and related processes on Pd/Ir hetero-metallene surface. E_{vac} = vacuum energy, E_c = conduction band, E_v = valence band, E_{f-m} = Fermi level of metal, E_{f-s} = Fermi level of support.

2.3. Characterizations

Transmission electron microscope (TEM), high-resolution TEM (HR-TEM), high-angle annular dark-field scanning transmission electron microscopy (HAADF-STEM), selected area electron diffraction (SAED), STEM energy dispersive X-ray spectroscopy (STEM-EDS) mapping images were collected on a JEM-2100 F (JEOL, Japan) with an accelerating voltage of 200 kV. X-ray diffraction (XRD) measurements were carried out on Ultima IV (Rigaku, Japan) with $\text{Cu K}\alpha$ radiation ($\lambda = 1.5406 \text{ \AA}$). X-ray photoelectron spectra (XPS) were acquired on K-Alpha (Thermo Scientific, USA). Atomic force microscopy (AFM) measurements were performed on MFP-3D Infinity (Asylum Research, USA) and were provided technical support by “Ceshigo Research Service, (www.ceshigo.com)”.

2.4. Electrochemical experiments

Electrochemical HER tests were performed in 0.5 M H_2SO_4 using a CHI 660E electrochemical workstation. In the HER experiment, a three-electrode system was assembled with a catalyst-covered glassy carbon electrode (GCE, 3 mm diameter, 0.071 cm^2) as the working electrode, Ag/AgCl as the reference electrode, and a carbon rod as the counter electrode. In preparing the ink solution, 2 mg of catalyst was dissolved with deionized water, ethanol, and nafion (0.05 wt%) in a ratio of 8:1:1. Then, 5 μL of ink solution was dropped on the GCE surface and dried in an oven at 60°C to prepare the working electrode. In this work, all of the electrochemical tests were carried out at ambient temperature and pressure. Linear sweep voltammetry (LSV) was performed in a N_2 -saturated 0.5 M H_2SO_4 electrolyte at a scan rate of 5 mV s^{-1} with 95% iR compensation. iR correction was carried out according to the following equation: $E_{corr} = E_{mea} - iR$ (where E_{corr} is the iR-compensated potential, E_{mea} is the experimentally measured potential, and R is the solution resistance (R_s)). The currents were normalized according to the geometric area of the working electrode (0.071 cm^2) to obtain HER current density data. In this work, all potentials were converted to reversible hydrogen electrode (RHE) according to the equation $E_{RHE} = E_{Ag/AgCl} + 0.2224 \text{ V} + 0.05916 \times \text{pH}$. In the high current density test, the working electrode was prepared by dispersing 200 μL of catalyst slurry (5 mg/L) on $1 \text{ cm} \times 1 \text{ cm}$ carbon paper. The accelerated durability test was performed by cyclic voltammetry (CV) with a scan rate of 200 V s^{-1} . The chronopotentiometry tests (V-t) were carried out at a constant current density of 250 mA cm^{-2} .

2.5. Hydrogen spillover experiment

The dried sample is placed in a closed container at room temperature. Then H_2 was slowly introduced and the changes were observed. The relationship between the position of the hydrogen desorption peak and the scan rate was tested using cyclic voltammetry (CV) for different catalysts ranging from 50 to 850 V s^{-1} in 0.5 M H_2SO_4 . Furthermore, the LSV polarization curves were tested in 0.5 M H_2SO_4 and 0.5 M D_2SO_4 solutions.

2.6. Density functional theory (DFT)

All the DFT calculations were conducted based on the Vienna Ab-initio Simulation Package (VASP). The exchange-correlation effects were described by the Perdew-Burke-Ernzerhof (PBE) functional within the generalized gradient approximation (GGA) method. The core-valence interactions were accounted by the projected augmented wave (PAW) method. The energy cutoff for plane wave expansions was set to 450 eV, and the $4 \times 4 \times 1$ Monkhorst-Pack grid k-points were selected to sample the Brillouin zone integration. The vacuum space is adopted about 12 \AA above the surfaces to avoid periodic interactions. The structural optimization was completed for energy and force convergence set at $1.0 \times 10^{-5} \text{ eV}$ and 0.01 eV \AA^{-1} , respectively.

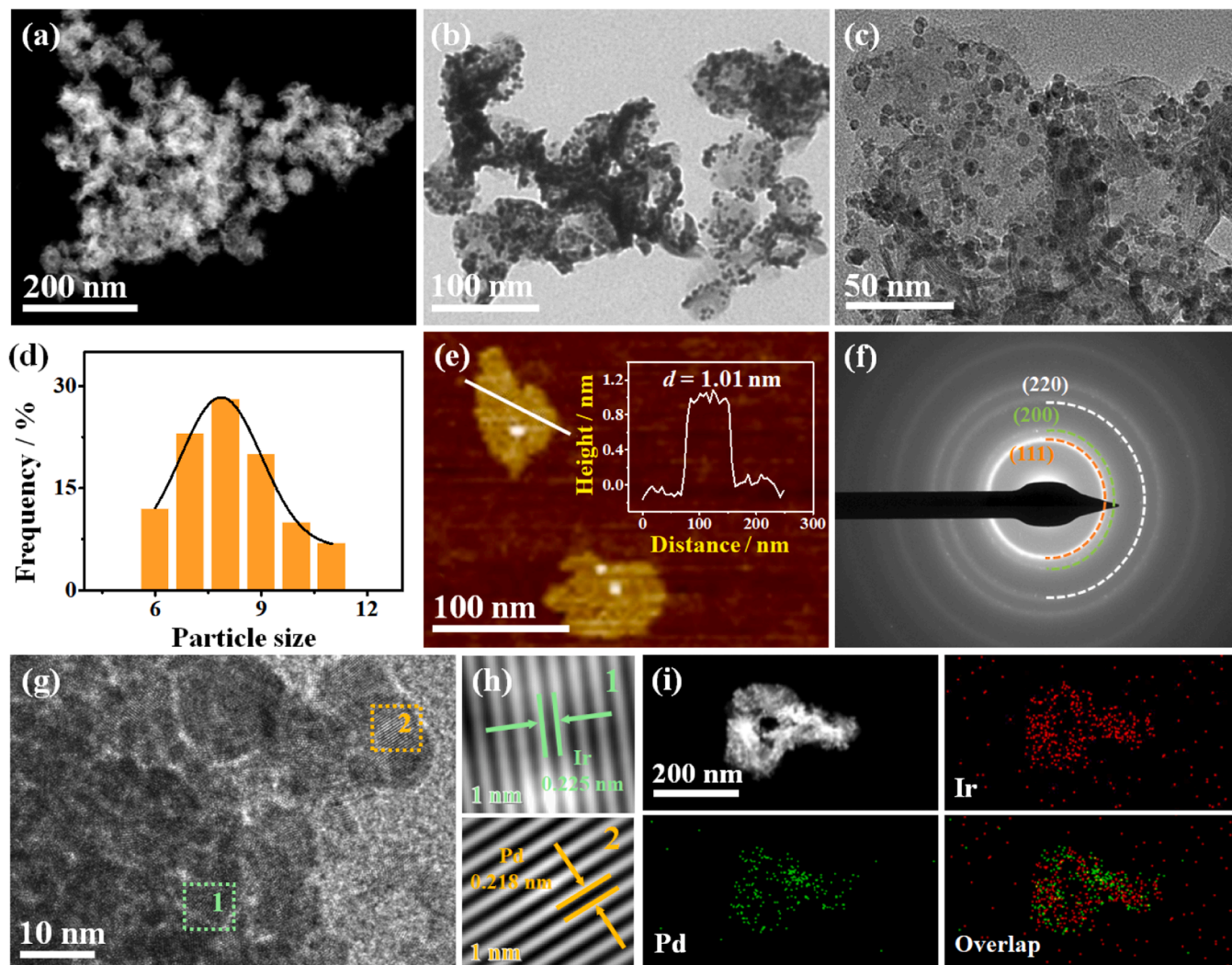


Fig. 2. (a) HAADF-STEM, (b) low magnification TEM and (c) high magnification TEM images of the Pd/Ir hetero-metallene. (d) Particle size distribution histogram of Pd on Pd/Ir hetero-metallene. (e) AFM image and the corresponding height profile. (f) SAED pattern of Pd/Ir hetero-metallene. (g) HRTEM image of Pd/Ir hetero-metallene and (h) the Fourier-filtered lattice pattern of the selected area in (g). (i) HAADF-STEM and corresponding element mapping images of the Pd/Ir hetero-metallene.

The Gibbs free energy changes (ΔG) of the reaction are calculated using the following formula:

$$\Delta G = \Delta H - T\Delta S = \Delta E_{DFT} + \Delta E_{ZPE} + \int_0^T C_V dT - T\Delta S$$

where ΔE is the electronic energy difference directly obtained from DFT calculations, ΔE_{ZPE} is the zero-point energy difference, T is the room temperature (298.15 K) and ΔS is the entropy change.

3. Results and discussion

3.1. Materials characterization

The E_f of the material plays a crucial role in determining the transfer kinetics of hydrogen spillover at the interface between the metal and the support [44]. Considering the quantitative relationship between E_f and the material work function (Φ) ($E_f = \Phi - E_{vac}$), the Φ_{Ir} and Φ_{Pd} were calculated by DFT. As shown in Fig. S1, the Φ_{Ir} is 5.66 eV, and the Φ_{Pd} is 4.9 eV, and the difference between them is only 0.76 eV. Mechanistic analysis and theoretical calculations show that the small $\Delta\Phi$ between Pd and Ir facilitates the hydrogen spillover from the metal (Pd) to the support (Ir), thus making the Pd/Ir hetero-metallene a potential efficient

HER electrocatalyst (Fig. 1). Pd/Ir hetero-metallene was prepared by a simple one-step co-reduction wet chemical method (Fig. S2). Low-magnification transmission electron microscopy (TEM), and high-angle annular dark-field scanning transmission electron microscopy (HAADF-STEM) images reveal that Pd/Ir hetero-metallene possesses a pronounced 2D graphene-like structure with transverse dimensions in the range of about a few hundred nanometers (Fig. 2a-b and Fig. S3). The Pd NPs were uniformly distributed on the Ir metallene surface with an average diameter of about 8.5 nm (Fig. 2c and d). In addition, the thickness of Pd/Ir hetero-metallene is about 1.01 nm as measured by atomic force microscopy (AFM), which indicates its ultrathin nature (Fig. 2e). The selected area electron diffraction (SAED) pattern of Pd/Ir hetero-metallene show continuous diffraction rings, suggesting its polycrystalline structure (Fig. 2f). The structural information of Pd/Ir hetero-metallene on the atomic scale was further analyzed by high resolution TEM images. As depicted in Fig. 2g and h, the lattice spacings of 0.225 and 0.218 nm are assigned to the face-centered cubic (fcc) (111) faces of Ir and Pd, respectively. STEM energy dispersive X-ray spectroscopy (STEM-EDS) mapping images further verified the homogeneous distribution of Pd on the Ir metallene surface and the Pd/Ir atomic ratio is 35.61/64.39 (Fig. 2i and Fig. S4). Moreover, Ir metallene and Pd NPs can be synthesized separately, where

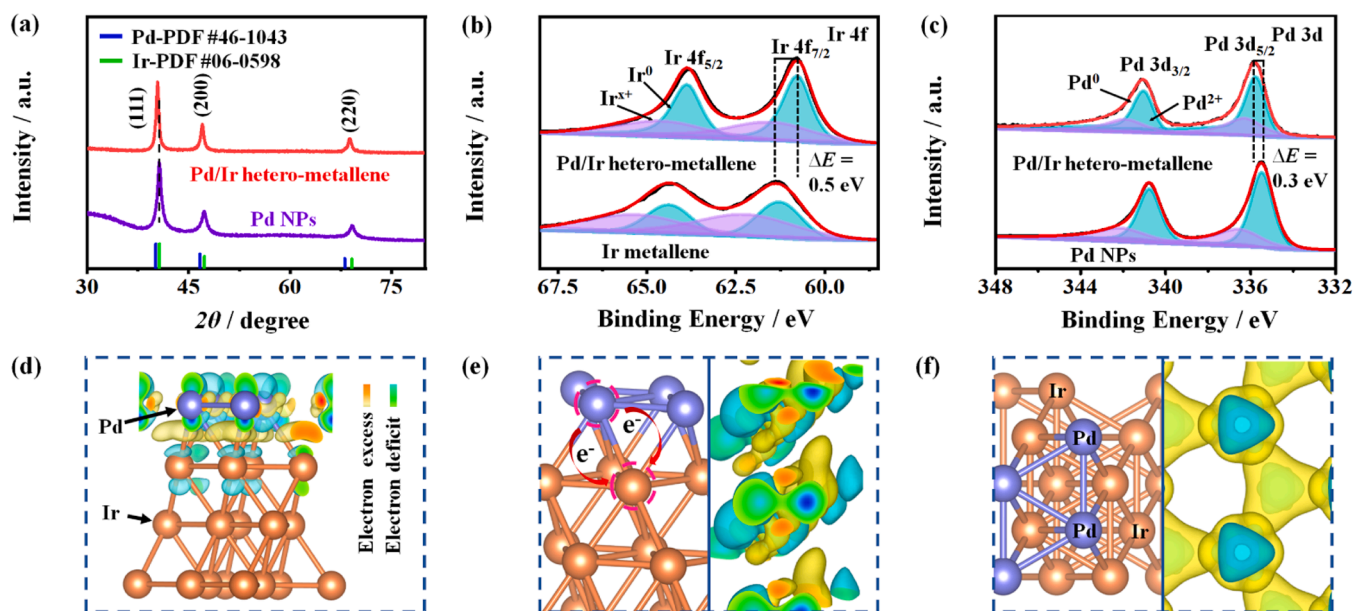


Fig. 3. (a) XRD patterns of the Pd/Ir hetero-metallene and Pd NPs. (b) Ir 4f XPS spectra of the Pd/Ir hetero-metallene and Ir metallene. (c) Pd 3d XPS spectra of the Pd/Ir hetero-metallene and Pd NPs. (d) Electron density difference on the Pd/Ir hetero-metallene. (e) Electron transport directions and (f) top view of electron density difference on the Pd/Ir hetero-metallene. Yellow areas indicate electron excess and cyan areas indicate electron deficiency.

Ir metallene maintains a 2D morphology, while Pd NPs exhibit a granular agglomerated structure (Fig. S5).

The crystal structure of as-prepared samples was performed by X-ray diffractometer (XRD). The Pd/Ir hetero-metallene exhibits a typical *fcc* structure (Fig. 3a), which is consistent with SAED result. Compared to the standard cards of Ir (No. 06-0598) and Pd (No. 46-1043), no significant phase separation was observed in Pd/Ir hetero-metallene, which can be attributed to the similarity of the crystal structures of Pd and Ir. Subsequently, the valence states of the elements were measured by X-ray photoelectron spectroscopy (XPS). The corresponding Pd/Ir hetero-metallene full spectrum clearly reveals that the sample consists mainly of two components, Ir and Pd (Fig. S6). In the XPS spectra of Ir 4f and Pd 3d, metallic and oxidized states of Ir and Pd species coexist, with the metallic state being the dominant phase (Fig. 3b and c). The Ir 4f_{7/2} peak of the Pd/Ir hetero-metallene is positively shifted by about 0.5 eV from that of Ir metallene, while the Pd 3d_{5/2} peak of the Pd/Ir hetero-metallene is negatively shifted by about 0.3 eV from that of the Pd NPs (Fig. 3b and c). The shifts in binding energies indicate significant Ir-Pd interactions and electron redistribution at the interface. The catalyst surface electronic properties of Pd/Ir hetero-metallene and Ir metallene were further characterized using ultraviolet photoelectron spectroscopy (UPS) as shown in Fig. S7a. The calculated Φ value of the Pd/Ir hetero-metallene (4.89 eV) is smaller than that of the Ir metallene (5.66 eV) (Fig. S7b), indicating a more balanced electron cloud density distribution for the Pd/Ir hetero-metallene. This may be due to the redistribution of charge between Pd and Ir at the Pd/Ir interface until the system reaches a more equilibrium state. To gain further insight into the charge density distribution in the Pd/Ir hetero-metallene, the Bader charge and charge density difference analysis was performed (Fig. 3d-f and Fig. S8-9). The electron deficiency around the Pd atoms and the electron enrichment around the Ir atoms can be observed at the interface, indicating a charge transfer from Pd to Ir, which is consistent with the XPS and UPS results. The change in electronic configuration further optimized the adsorption/desorption of reactants, intermediates, and products during the electrocatalytic process, thus improving the performance.

3.2. HER performance of Pd/Ir hetero-metallene in acid electrolytes

Linear sweep voltammetry (LSV) curves of Pd/Ir hetero-metallene, Ir metallene, Pd NPs and Pt/C were tested in 0.5 M H₂SO₄ acid electrolyte. The LSV curve of Pd NPs starts with a large hydrogen adsorption peak due to the strong adsorption of H⁺ on the Pd surface (Fig. 4a). The formation of a strong Pd-H_{ads} adsorption state results in a large kinetic energy barrier to overcome for H_{ads} desorption, thus limiting the intrinsic HER activity. The regulation effect of element Ir on the Pd site is obvious. After the addition of Ir, the adsorption peak of Pd-H_{ads} is weakened, and H_{ads} can be rapidly separated from Pd site, thus improving the HER activity (Fig. 4a). As a result, Pd/Ir hetero-metallene exhibits excellent HER catalytic activity, requiring only 21 mV to reach a current density of 10 mA cm⁻², which is much lower than that of Pd NPs (38 mV), Ir metallene (49 mV) and Pt/C (34 mV) (Fig. 4b). The HER activity of Pd/Ir hetero-metallene was also superior to that of most of the reported Pd and Ir-based electrocatalysts (Table S1). The Tafel slope values of the catalysts were calculated from the LSV curves to reveal the HER kinetics. The Tafel slope for Pd/Ir hetero-metallene is 21.0 mV dec⁻¹, lower than that of Pd NPs (66.7 mV dec⁻¹), Ir metallene (44.6 mV dec⁻¹) and Pt/C (39.0 mV dec⁻¹), suggesting a rapid HER kinetics (Fig. 4c). Based on the theoretical values of Volmer (120 mV dec⁻¹), Heyrovsky (40 mV dec⁻¹), and Tafel (30 mV dec⁻¹) reactions in the rate-determining step (RDS) [45], it was concluded that the RDS for Pd/Ir hetero-metallene is consistent with the Tafel pathway. This mechanistic shift means that adsorption of active hydrogen at the Pd site no longer determines the rate of HER, and H_{ad} desorption begins to limit the rate of the overall reaction. The introduction of Ir accelerates the HER kinetics, which may be due to the hydrogen spillover effect that promotes H_{ads} transfer and reduces the adsorption energy of the Pd-H_{ads} band. Kinetic isotope effect (KIE) is often used as a proton transfer rate descriptor to estimate the proton transfer involved in the RDS of an electrocatalytic reaction. LSV curves of Pd/Ir hetero-metallene were determined in 0.5 M D₂SO₄/D₂O and 0.5 M H₂SO₄/H₂O solutions, and the corresponding KIE values were calculated from the ratio of current densities of H₂O and D₂O electrolytes at selected potentials (j_{H+}/j_{D+}) (Fig. 4d and e). When the KIE value is greater than 1.5, it can be inferred that proton or proton transfer is indeed affecting the RDS [46,47]. The measured KIE values of Pd/Ir hetero-metallene vary from 7.3 to 14 at the

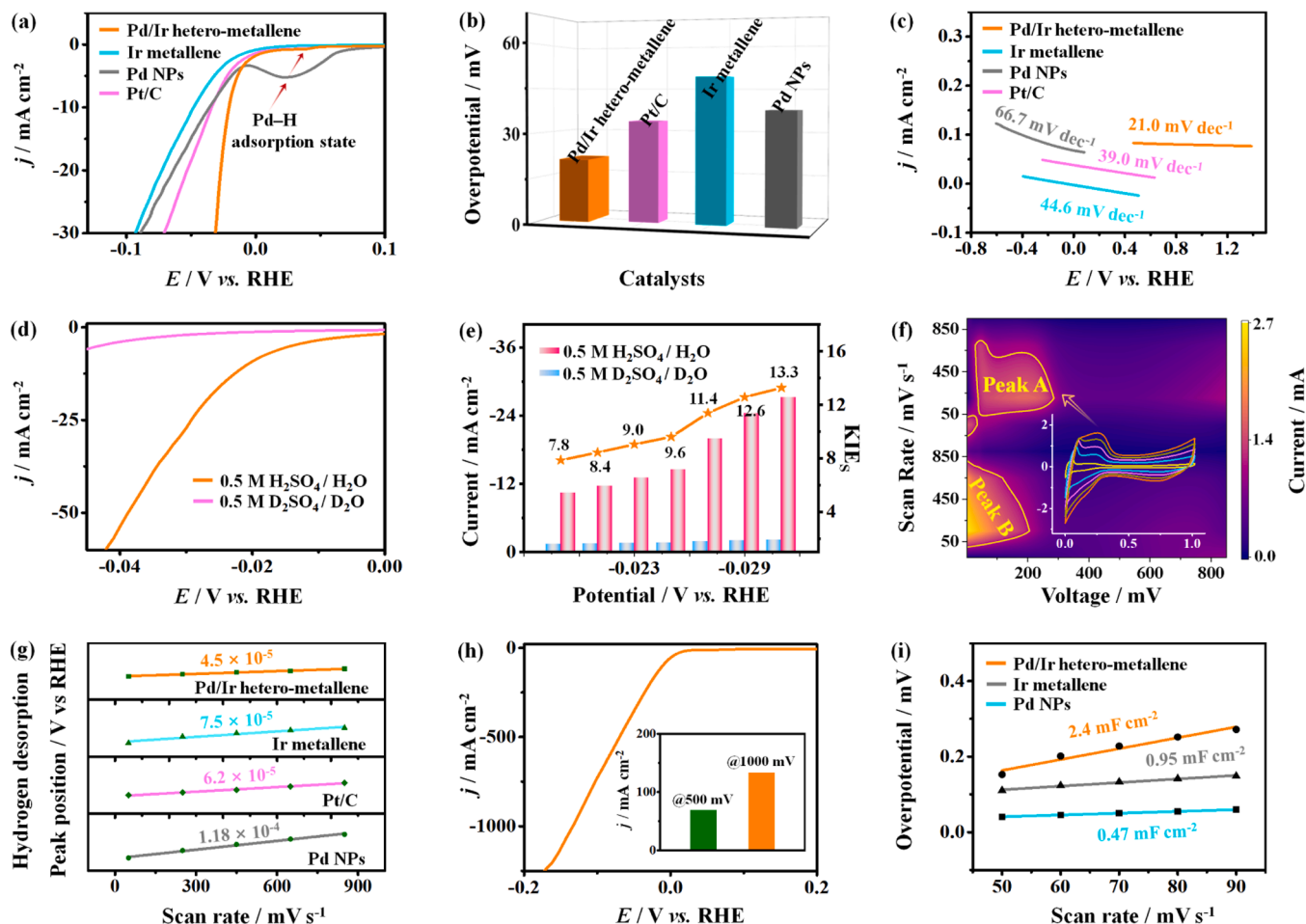


Fig. 4. (a) HER polarization curves, (b) the comparison of overpotentials at 10 mA cm^{-2} , and (c) Tafel plots for various samples. (d) Polarization curves of Pd/Ir hetero-metallene in $0.5 \text{ M H}_2\text{SO}_4/\text{H}_2\text{O}$ and $0.5 \text{ M D}_2\text{SO}_4/\text{D}_2\text{O}$ solutions. (e) Calculated KIE values under corresponding potentials from (d). (f) Contour plots of CV pattern of Pd/Ir hetero-metallene with the scan rate from 50 to 850 mV s^{-1} . (g) Plots of hydrogen desorption peak position vs. scan rates. (h) LSV curve of Pd/Ir hetero-metallene at ampere-level current densities and the comparison of overpotentials at 500 mA cm^{-2} and 1000 mA cm^{-2} . (i) double-layer capacitances (C_{dl}) of Pd/Ir hetero-metallene, Ir metallene and Pd NPs.

corresponding potentials (-0.02 to -0.35 vs. RHE). The larger KIE value for Pd/Ir hetero-metallene (>1.5) may reflect the effect of proton or hydrogen transfer on the reaction rate, which is consistent with the fact that Pd and Ir hybridization promotes hydrogen spillover.

3.3. Confirmation of hydrogen spillover in Pd/Ir hetero-metallene

In order to verify the hydrogen spillover phenomenon in Pd/Ir hetero-metallene, WO_3 was physically mixed with catalyst powder and placed in an airtight container at room temperature, and then H_2 was slowly introduced. As shown in the Fig. S10, the yellow WO_3 powder turns dark blue rapidly under a H_2 atmosphere, which indicates the hydrogen spillover effect in Pd/Ir hetero-metallene electrocatalysts. As a comparison, the Ir metallene mixture turns blue while the Pd NPs remained unchanged, which again proves that Pd has a strong adsorption of hydrogen, and is not conducive to hydrogen spillover. To further confirm the hydrogen spillover phenomenon, the cyclic voltammetry (CV) curves at different scan rates were recorded to quantify their hydrogen desorption kinetics. Fig. 4f shows the contour plots of the CV diagrams for Pd/Ir hetero-metallene. The two peak A and peak B correspond to the hydrogen desorption and adsorption peaks. It was found that the hydrogen desorption peaks of Pd/Ir hetero-metallene, Ir metallene, Pd NPs and Pt/C were positively shifted with increasing scanning speed (Fig. 4f and Fig. S11). The fitted slope of Pd/Ir hetero-metallene is 4.5×10^{-5} , which is lower than that of Ir metallene (7.5

$\times 10^{-5}$) and Pd NPs (1.18×10^{-4}), suggesting that Pd/Ir hetero-metallene is more likely to desorb H_{ads} relative to Ir metallene and Pd NPs (Fig. 4g). For metal-supported heterojunction electrocatalysts, the electrolytic desorption of hydrogen could be accelerated by hydrogen spillover [24,27]. Apparently, the slope of Pd/Ir hetero-metallene decreases dramatically indicating a significant acceleration of the hydrogen desorption kinetics. It can be concluded that the hydrogen transfer from Pd to Ir was successfully realized in Pd/Ir hetero-metallene, thus improving the intrinsic catalytic activity of Pd.

The change in HER performance due to the hydrogen spillover effect is not only reflected in low-current densities, but also shows excellent performance at ampere-level current densities. As shown in Fig. 4h, the Pd/Ir hetero-metallene exhibits an ultra-low overpotentials of only 69 and 133 mV to reach 500 and 1000 mA cm^{-2} . Electrochemical active surface area (ECSA) is an important index for evaluating the electrocatalytic performance of catalysts, and it is linearly related to the magnitude of double layer capacitance (C_{dl}). The C_{dl} values of 2.4 mF cm^{-2} , 0.47 mF cm^{-2} and 0.95 mF cm^{-2} are calculated for Pd/Ir hetero-metallene, Ir metallene and Pd NPs, respectively (Fig. 4i and Fig. S12). According to the C_{dl} value (assuming a specific capacitance of $40 \mu\text{F cm}^{-2}$), the ECSAs for Pd/Ir hetero-metallene, Ir metallene and Pd NPs were calculated to be 60.00 , 11.75 and 23.75 cm^{-2} , respectively. The Pd/Ir hetero-metallene has the largest ECSA, probably due to its unique metallene morphology and the heterogeneous interfacial structure formed by the interaction of the two metals. In addition to activity, the

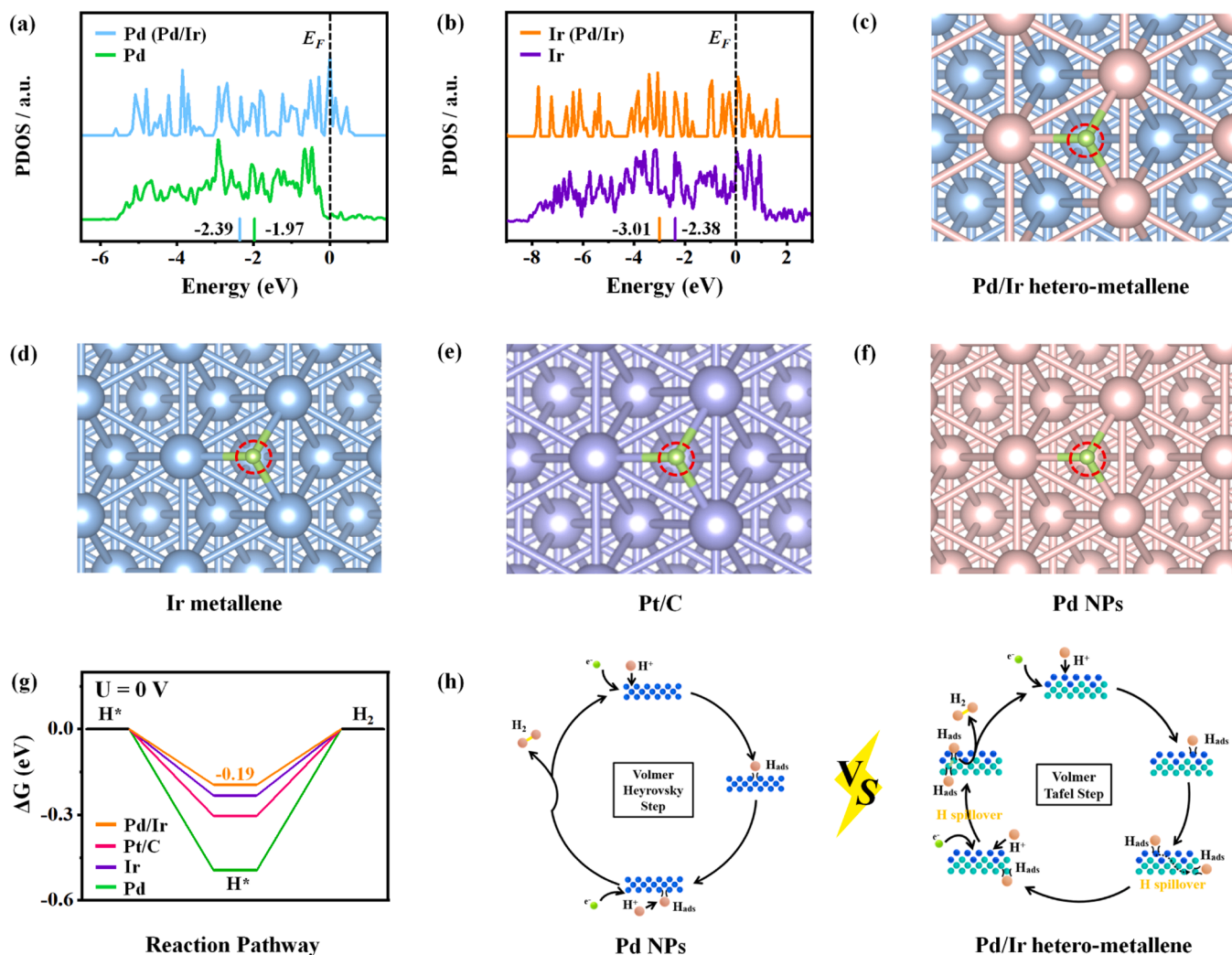


Fig. 5. (a and b) Comparison of d orbital distribution between Pd/Ir hetero-metallene and Ir or Pd. (c-f) The top views of the optimized structure of H_{ads} absorbed for Pd/Ir hetero-metallene, Pt/C, Ir metallene and Pd NPs. The blue, pink, purple and green balls represent Ir, Pd, Pt and H atoms, respectively. (g) Calculated hydrogen free energy curves of HER for Pd/Ir hetero-metallene, Pt/C, Ir metallene and Pd NPs. (h) Diagram of reaction pathway transformation due to hydrogen spillover effect.

stability of the catalyst is an important indicator. After 5000 CV cycles, it can be seen from Fig. S13a that the HER activity of Pd/Ir hetero-metallene has not been significantly weakened. Moreover, the Pd/Ir hetero-metallene showed good stability at 250 mA cm^{-2} during 100 h chronopotentiometry test (V-t) (Fig. S13b). The TEM images of Pd/Ir hetero-metallene after stability testing also did not observe significant particle size differences and agglomeration (Fig. S14). All these tests proved that Pd/Ir hetero-metallene is well stabilized during the HER process.

3.4. DFT calculations

To further explore the intrinsic reasons for the enhanced HER catalytic performance of Pd/Ir hybrid-metallene in acidic electrolytes, the electronic density of states (DOS) of all the samples were calculated (Fig. 5a-b). The d -band center energy of Pd is negatively shifted to a lower energy near the E_F with the presence of Ir (Fig. 5a). The downshifted of the d -band center helps to weaken the overly strong adsorption H_{ads} on the Pd site, thus accelerating the transfer of adsorbed H_{ads} in the HER process and improving the catalytic efficiency. In addition, DFT calculations were further performed using the PdIr (111) surface as a model (Fig. 5c). For comparison, the Pd (111), Ir (111) and Pt (111) planes representing Ir metallene, Pd NPs and Pt/C, respectively, were

also studied (Fig. 5d-f). The HER process of Pd/Ir hybrid-metallene in acidic solutions follows the Volmer-Tafel mechanism which consists of several steps, i.e., adsorption of H^+ to form H_{ads} , binding of H_{ads} to produce adsorbed H_2 , and finally desorption of H_2 . As an ideal HER, its $\Delta G_{H_{ads}}$ should be neither too strong nor too weak, which is a good descriptor for evaluating the ability of a material to catalyze HER. For Pd NPs, $\Delta G_{H_{ads}}$ on the surface of Pd (111) was calculated to be -0.49 eV , indicating a strong Pd- H_{ads} adsorption and a limited H_{ads} desorption (Fig. 5g). In contrast, the $\Delta G_{H_{ads}}$ of Pd/Ir hybrid-metallene (-0.19 eV) is much lower than that of Ir metallene (-0.23 eV), Pd NPs (-0.49 eV), and Pt/C (-0.3 eV), which would enable the rapid adsorption of H^+ and release of H_2 , thus greatly contributing to the superior HER performance (Fig. 5g). All experimental tests and theoretical calculations showed that Pd NPs anchored on Ir metallene carriers effectively adjusted the charge redistribution of the Pd sites, accelerated the electron transfer, produced the hydrogen spillover phenomenon, tuned the RDS, and improved the performance of Pd/Ir hybrid-metallene against HER (Fig. 5h).

4. Conclusion

In summary, the Pd/Ir hetero-metallene were successfully prepared using a facile one-step method, in which the Pd NPs were uniformly distributed on the ultrathin 2D Ir metallene. A combination of structural

characterization, electrochemical properties, kinetic analysis, and theoretical calculations to understand the adsorption and desorption behavior of H_{ads} demonstrates the existence of hydrogen spillover between the Pd and Ir interfaces. The addition of Ir weakens the excessively strong H_{ads} adsorption on the Pd site and makes Pd- H_{ads} easily desorbed with the aid of hydrogen spillover at the Pd-Ir interfaces, resulting in superior HER performance. This work provides new perspectives for the design of advanced heterojunction metal-support catalysts that can be used in for industrial-scale H_2 production.

CRedit authorship contribution statement

Hongjie Yu: Writing – review & editing. **Qiqi Mao:** Writing – review & editing. **Liang Wang:** Writing – review & editing. **Ziqiang Wang:** Writing – review & editing. **Hongjing Wang:** Supervision, Funding acquisition. **Zilong Lian:** Writing – review & editing. **Kai Deng:** Writing – review & editing, Writing – original draft, Data curation. **Jiabao Yu:** Writing – review & editing. **Wenxin Wang:** Writing – review & editing.

Declaration of Competing Interest

The authors declare that they have no known competing financial interests or personal relationships that could have appeared to influence the work reported in this paper.

Data availability

Data will be made available on request.

Acknowledgments

This work was financially supported by the National Natural Science Foundation of China (Nos. 22372148, 22278369, 21972126, 22308330 and 21978264) and Natural Science Foundation of Zhejiang Province (Nos. LR24B060001, LQ22B030012 and LQ23B030010).

Appendix A. Supporting information

Supplementary data associated with this article can be found in the online version at [doi:10.1016/j.apcatb.2024.124047](https://doi.org/10.1016/j.apcatb.2024.124047).

References

- [1] Z. Zhu, X. Yang, J. Liu, M. Zhu, X. Xu, Handily etching nickel foams into catalyst–substrate fusion self-stabilized electrodes toward industrial-level water electrolysis, *Carbon Energy* 5 (2023) e327, <https://doi.org/10.1002/cey2.327>.
- [2] T. Liu, W. Gao, Q. Wang, M. Dou, Z. Zhang, F. Wang, Selective loading of atomic platinum on a RuCeO_x support enables stable hydrogen evolution at high current densities, *Angew. Chem. Int. Ed.* 59 (2020) 20423–20427, <https://doi.org/10.1002/anie.202009612>.
- [3] Q. Zhou, R. Sun, Y. Ren, R. Tian, J. Yang, H. Pang, K. Huang, X. Tian, L. Xu, Y. Tang, Reactive template-derived interfacial engineering of CoP/CoO heterostructured porous nanotubes towards superior electrocatalytic hydrogen evolution, *Carbon Energy* 5 (2022) e273, <https://doi.org/10.1002/cey2.273>.
- [4] Y. Li, C. Peng, H. Hu, S. Chen, J. Choi, Y. Lin, J. Lee, Interstitial boron-triggered electron-deficient Os aerogels for enhanced pH-universal hydrogen evolution, *Nat. Commun.* 13 (2022) 1143, <https://doi.org/10.1038/s41467-022-28805-8>.
- [5] Y.-Z. Wang, M. Yang, Y. Ding, N. Li, L. Yu, Recent advances in complex hollow electrocatalysts for water splitting, *Adv. Funct. Mater.* 32 (2021) 2108681, <https://doi.org/10.1002/adfm.202108681>.
- [6] Q. Mao, W. Wang, K. Deng, H. Yu, Z. Wang, Y. Xu, X. Li, L. Wang, H. Wang, Low-content Pt-triggered the optimized d-band center of Rh metallene for energy-saving hydrogen production coupled with hydrazine degradation, *J. Energy Chem.* 85 (2023) 58–66, <https://doi.org/10.1016/j.jechem.2023.06.005>.
- [7] V. Jose, V. Do, P. Prabhhu, C. Peng, S. Chen, Y. Zhou, Y. Lin, J. Lee, Activating amorphous Ru metallenes through Co integration for enhanced water electrolysis, *Adv. Energy Mater.* 13 (2023) 2301119, <https://doi.org/10.1002/aenm.202301119>.
- [8] J. Tian, Y. Hu, W. Lu, J. Zhu, X. Liu, J. Shen, G. Wang, J. Schroers, Dealloying of an amorphous TiCuRu alloy results in a nanostructured electrocatalyst for hydrogen evolution reaction, *Carbon Energy* 5 (2023) e322, <https://doi.org/10.1002/cey2.322>.
- [9] P. Kuang, Z. Ni, B. Zhu, Y. Lin, J. Yu, Modulating the d-Band center enables ultrafine Pt₃Fe alloy nanoparticles for pH-universal hydrogen evolution reaction, *Adv. Mater.* 35 (2023) e2303030, <https://doi.org/10.1002/adma.202303030>.
- [10] R. Wan, M. Luo, J. Wen, S. Liu, X. Kang, Y. Tian, Pt-Co single atom alloy catalysts: accelerated water dissociation and hydrogen evolution by strain regulation, *J. Energy Chem.* 69 (2022) 44–53, <https://doi.org/10.1016/j.jechem.2021.12.045>.
- [11] Y. Guo, B. Hou, X. Cui, X. Liu, X. Tong, N. Yang, Pt atomic layers boosted hydrogen evolution reaction in nonacidic media, *Adv. Energy Mater.* 12 (2022) 2201548, <https://doi.org/10.1002/aenm.202201548>.
- [12] J.N. Tiwari, S. Sultan, C.W. Myung, T. Yoon, N. Li, M. Ha, A.M. Harzandi, H. J. Park, D.Y. Kim, S.S. Chandrasekaran, W.G. Lee, V. Vij, H. Kang, T.J. Shin, H. S. Shin, G. Lee, Z. Lee, K.S. Kim, Multicomponent electrocatalyst with ultralow Pt loading and high hydrogen evolution activity, *Nat. Energy* 3 (2018) 773–782, <https://doi.org/10.1038/s41560-018-0209-x>.
- [13] Q. Mao, W. Wang, K. Deng, H. Yu, Z. Wang, Y. Xu, X. Li, L. Wang, H. Wang, Low-content Pt-triggered the optimized d-band center of Rh metallene for energy-saving hydrogen production coupled with hydrazine degradation, *J. Energy Chem.* 85 (2023) 58–66, <https://doi.org/10.1016/j.jechem.2023.06.005>.
- [14] Z. Wang, B. Xiao, Z. Lin, Y. Xu, Y. Lin, F. Meng, Q. Zhang, L. Gu, B. Fang, S. Guo, W. Zhong, PtSe₂/Pt heterointerface with reduced coordination for boosted hydrogen evolution reaction, *Angew. Chem. Int. Ed.* 60 (2021) 23388–23393, <https://doi.org/10.1002/anie.202110335>.
- [15] R. Subbaraman, D. Tripkovic, D. Strmcnik, K. Chang, M. Uchiumura, A.P. Paulikas, V. Stamenkovic, N.M. Markovic, Enhancing hydrogen evolution activity in water splitting by tailoring Li⁺-Ni(OH)₂-Pt interfaces, *Science* 334 (2011) 1256–1260, <https://doi.org/10.1126/science.1211934>.
- [16] H. Cao, Q. Wang, Z. Zhang, H. Yan, H. Zhao, H.B. Yang, B. Liu, J. Li, Y. Wang, Engineering single-atom electrocatalysts for enhancing kinetics of acidic volmer reaction, *J. Am. Chem. Soc.* 145 (2023) 13038–13047, <https://doi.org/10.1021/jacs.2c13418>.
- [17] F. Zaar, C.M. Araujo, R. Emanuelsson, M. Stromme, M. Sjödin, Tetraphenylporphyrin electrocatalysts for the hydrogen evolution reaction: applicability of molecular volcano plots to experimental operating conditions, *Dalton Trans.* 52 (2023) 10348–10362, <https://doi.org/10.1039/d3dt01250f>.
- [18] P. Sabatier, Hydrogénations et déshydrogénations par catalyse, *Ber. Dtsch. Chem. Ges.* 44 (2006) 1984–2001, <https://doi.org/10.1002/cber.19110440303>.
- [19] M. Yan, R. Wei, R. Zhang, X. Zhang, S. Sun, X. Wei, X. Wang, S. Yin, Y. Wang, Distinctive p-d orbital hybridization in CuSb porous nanonetworks for enhanced nitrite electroreduction to ammonia, *Small* (2024) 2310409, <https://doi.org/10.1002/smll.202310409>.
- [20] M. Xiong, Z. Gao, Y. Qin, Spillover in heterogeneous catalysis: new insights and opportunities, *ACS Catal.* 11 (2021) 3159–3172, <https://doi.org/10.1021/acscatal.0c05567>.
- [21] J. Chen, C. Chen, M. Qin, B. Li, B. Lin, Q. Mao, H. Yang, B. Liu, Y. Wang, Reversible hydrogen spillover in Ru-WO_{3-x} enhances hydrogen evolution activity in neutral pH water splitting, *Nat. Commun.* 13 (2022) 5382, <https://doi.org/10.1038/s41467-022-33007-3>.
- [22] Y. Liu, Y. Chen, Y. Tian, T. Sakthivel, H. Liu, S. Guo, H. Zeng, Z. Dai, Synergizing hydrogen spillover and deprotonation by the internal polarization field in a MoS₂/NiPS₃ vertical heterostructure for boosted water electrolysis, *Adv. Mater.* 34 (2022) e2203615, <https://doi.org/10.1002/adma.202203615>.
- [23] H.Q. Fu, M. Zhou, P.F. Liu, P. Liu, H. Yin, K.Z. Sun, H.G. Yang, A. Mohammad, P. Hu, H. Wang, H. Zhao, Hydrogen spillover-bridged volmer/tafel processes enabling ampere-level current density alkaline hydrogen evolution reaction under low overpotential, *J. Am. Chem. Soc.* 144 (2022) 6028–6039, <https://doi.org/10.1021/jacs.2c01094>.
- [24] Y. Tan, Y. Zhu, X. Cao, Y. Liu, J. Li, Z. Chen, J. Hu, Discovery of hydrogen spillover-based binary electrocatalysts for hydrogen evolution: from theory to experiment, *ACS Catal.* 12 (2022) 11821–11829, <https://doi.org/10.1021/acscatal.2c02594>.
- [25] J. Li, Y. Tan, M. Zhang, W. Guo, S. Zhang, Y. Ma, J. Hu, Y. Qu, Boosting electrocatalytic activity of Ru for acidic hydrogen evolution through hydrogen spillover strategy, *ACS Energy Lett.* 7 (2022) 1330–1337, <https://doi.org/10.1021/acsenenergylett.1c02769>.
- [26] C. Mu, H. Xin, Q. Luo, Y. Li, F. Ma, Fabrication of Ru nanoclusters on Co-doped NiSe nanorods with efficient electrocatalytic activity towards alkaline hydrogen evolution via hydrogen spillover effect, *J. Mater. Chem. A* 11 (2023) 7016–7024, <https://doi.org/10.1039/d3ta00600j>.
- [27] J. Li, J. Hu, M. Zhang, W. Gou, S. Zhang, Z. Chen, Y. Qu, Y. Ma, A fundamental viewpoint on the hydrogen spillover phenomenon of electrocatalytic hydrogen evolution, *Nat. Commun.* 12 (2021) 3502, <https://doi.org/10.1038/s41467-021-23750-4>.
- [28] Z. Fan, F. Liao, Y. Ji, Y. Liu, H. Huang, D. Wang, K. Yin, H. Yang, M. Ma, W. Zhu, M. Wang, Z. Kang, Y. Li, M. Shao, Z. Hu, Q. Shao, Coupling of nanocrystal hexagonal array and two-dimensional metastable substrate boosts H₂-production, *Nat. Commun.* 13 (2022) 5828, <https://doi.org/10.1038/s41467-022-33512-5>.
- [29] T. Jian, L. Yu, Z. Zhao, W. Wu, Z. Wang, N. Cheng, Regulating the intermediate affinity on Pd nanoparticles through the control of inserted-B atoms for alkaline hydrogen evolution, *Chem. Eng. J.* 433 (2022) 133525, <https://doi.org/10.1016/j.cej.2021.133525>.
- [30] K. Deng, Z. Lian, W. Wang, J. Yu, H. Yu, Z. Wang, Y. Xu, L. Wang, H. Wang, Lattice strain and charge redistribution of Pt cluster/Ir metallene heterostructure for ethylene glycol to glycolic acid conversion coupled with hydrogen production, *Small* 20 (2024) 2305000, <https://doi.org/10.1002/smll.202305000>.
- [31] Z. Ren, H. Jiang, M. Yuan, Z. Xie, L. Deng, J. Han, K. Lyu, Y. Zhu, X. Li, L. Zhuang, Si regulation of hydrogen adsorption on nanoporous PdSi hybrids towards

- enhancing electrochemical hydrogen evolution activity, *Inorg. Chem. Front.* 10 (2023) 1101–1111, <https://doi.org/10.1039/d2qi02182j>.
- [32] K. Yeo, K. Lee, H. Kim, J. Lee, S. Kim, A highly active and stable 3D dandelion spore-structured self-supporting Ir-based electrocatalyst for proton exchange membrane water electrolysis fabricated using structural reconstruction, *Energy Environ. Sci.* 15 (2022) 3449–3461, <https://doi.org/10.1039/d2ee01042a>.
- [33] Z. Pu, J. Zhao, I.S. Amiinu, W. Li, M. Wang, D. He, S. Mu, A universal synthesis strategy for P-rich noble metal diphosphide-based electrocatalysts for the hydrogen evolution reaction, *Energy Environ. Sci.* 12 (2019) 952–957, <https://doi.org/10.1039/c9ee00197b>.
- [34] K. Deng, W. Wang, Z. Lian, H. Yu, Z. Wang, Y. Xu, H. Wang, L. Wang, A general synthesis of crystal phase controllable aerogels for efficient hydrogen evolution, *Small* (2023) e2304181, <https://doi.org/10.1002/smll.202304181>.
- [35] K. Deng, T. Zhou, Q. Mao, S. Wang, Z. Wang, Y. Xu, X. Li, H. Wang, L. Wang, Surface engineering of defective and porous Ir metallene with polyallylamine for hydrogen evolution electrocatalysis, *Adv. Mater.* 34 (2022) 2110680, <https://doi.org/10.1002/adma.202110680>.
- [36] X. Wang, J. Zhang, Z. Wang, Z. Lin, S. Shen, W. Zhong, Fabricating Ru single atoms and clusters on CoP for boosted hydrogen evolution reaction, *Chin. J. Struct. Chem.* 42 (2023) 100035, <https://doi.org/10.1016/j.cjsc.2023.100035>.
- [37] M. Luo, Z. Zhao, Y. Zhang, Y. Sun, Y. Xing, F. Lv, Y. Yang, X. Zhang, S. Hwang, Y. Qin, J. Ma, F. Lin, D. Su, G. Lu, S. Guo, PdMo bimetallic for oxygen reduction catalysis, *Nature* 574 (2019) 81–85, <https://doi.org/10.1038/s41586-019-1603-7>.
- [38] X. Liu, Y. Jiang, J. Huang, W. Zhong, B. He, P. Jin, Y. Chen, Bifunctional PdPt bimetallics for formate oxidation-boosted water electrolysis, *Carbon Energy* (2023) e367, <https://doi.org/10.1002/cey2.367>.
- [39] X. Zhang, R. Wei, M. Yan, X. Wang, X. Wei, Y. Wang, L. Wang, J. Zhang, S. Yin, One-pot synthesis inorganic-organic hybrid PdNi bimetallics for PET electrocatalytic value-added transformation, *Adv. Funct. Mater.* (2024) 2401796, <https://doi.org/10.1002/adfm.202401796>.
- [40] P. Prabhu, J. Lee, Metallenes as functional materials in electrocatalysis, *Chem. Soc. Rev.* 50 (2021) 6700–6719, <https://doi.org/10.1039/d0cs01041c>.
- [41] Q. Mao, X. Mu, W. Wang, K. Deng, H. Yu, Z. Wang, Y. Xu, L. Wang, H. Wang, Atomically dispersed Cu coordinated Rh metallene arrays for simultaneously electrochemical aniline synthesis and biomass upgrading, *Nat. Commun.* 14 (2023) 5679, <https://doi.org/10.1038/s41467-023-41423-2>.
- [42] P. Prabhu, V. Do, C.K. Peng, H. Hu, S. Chen, J. Choi, Y. Lin, J. Lee, Oxygen-bridged stabilization of single atomic W on Rh metallenes for robust and efficient pH-universal hydrogen evolution, *ACS Nano* 17 (2023) 10733–10747, <https://doi.org/10.1021/acsnano.3c02066>.
- [43] Y. Jiang, J. Leng, S. Zhang, T. Zhou, M. Liu, S. Liu, Y. Gao, J. Zhao, L. Yang, L. Li, W. Zhao, Modulating water splitting kinetics via charge transfer and interfacial hydrogen spillover effect for robust hydrogen evolution catalysis in alkaline media, *Adv. Sci.* (2023) e2302358, <https://doi.org/10.1002/adv.202302358>.
- [44] J. Li, Y. Tan, M. Zhang, W. Gou, S. Zhang, Y. Ma, J. Hu, Y. Qu, Boosting electrocatalytic activity of Ru for acidic hydrogen evolution through hydrogen spillover strategy, *ACS Energy Lett.* 7 (2022) 1330–1337, <https://doi.org/10.1021/acseenergylett.1c02769>.
- [45] B.E. Conway, B.V. Tilak, Interfacial processes involving electrocatalytic evolution and oxidation of H₂, and the role of chemisorbed H, *Electrochim. Acta* 47 (2002) 3571–3594, [https://doi.org/10.1016/s0013-4686\(02\)00329-8](https://doi.org/10.1016/s0013-4686(02)00329-8).
- [46] A.L. Andralojc, D.C. Grills, J. Zhang, R.M. Bullock, A. Miyazawa, Y. Kawanishi, E. Fujita, Kinetic and mechanistic studies of carbon-to-metal hydrogen atom transfer involving Os-centered radicals: evidence for tunneling, *J. Am. Chem. Soc.* 136 (2014) 3572–3578, <https://doi.org/10.1021/ja4123076>.
- [47] H. Li, F. Xie, M. Zhang, Metal-free electrocatalyst for water oxidation initiated by hydrogen atom transfer, *ACS Catal.* 11 (2020) 68–73, <https://doi.org/10.1021/acscatal.0c04606>.